Electronic Supplementary Material (ESI) for Energy & Environmental Science.
This journal is © The Royal Society of Chemistry 2022

All-scale Hierarchical Nanostructures and Superior Valence Band Convergence Lead to Ultra-high Thermoelectric Performance in Cubic GeTe

Debattam Sarkar,[1] Manisha Samanta,[1] Tanmoy Ghosh,[1] Kapildeb Dolui,[2] Subarna Das,[1] Kumar Saurabh,[1] Dirtha Sanyal,[3] and Kanishka Biswas[1,*]

[1]New Chemistry Unit, International Centre for Materials Science, School of Advanced Materials, Jawaharlal Nehru Centre for Advanced Scientific Research (JNCASR), Jakkur P.O., Bangalore 560064, India.

[2]Department of Physics and Astronomy, University of Delaware, Newark, Delaware 19716, USA

[3]Variable Energy Cyclotron Centre, 1/AF Bidhannagar, Kolkata 700064, India

**E-mail address: kanishka@jncasr.ac.in*

Methods

Reagents. Germanium (Ge, Strategy Elements, 99.999 %), tellurium (Te, Strategy Elements, 99.99 %) and antimony (Sb, Alfa Aesar, 99.9999 %) were used for synthesis of all the compounds.

Synthesis. High quality polycrystalline ingots of GeTe and $Ge_{0.9}Sb_{0.1}Te$ were synthesized by mixing stoichiometric amounts of high purity starting elements Ge, Te and Sb in quartz tubes which were then sealed under vacuum (10^{-6} Torr). The evacuated quartz tubes were then slowly heated to 1223 K and soaked at 1223 K for 6 hours, followed by slow cooling to room temperature over 10 h. To ensure phase homogeneity, the quartz tubes were shaken several times during soaking at high temperature. The obtained ingot of $Ge_{0.9}Sb_{0.1}Te$ was crushed into fine powder and was ball milled in FRITSCH PULVERISETTE 7 premium line planetary ball miller (with a spinning speed of 550 rpm) using stainless steel grinding bowls and balls for 150 minutes. Ball milled powder was then consolidated into cylinder by spark plasma sintering (SPS) (Dr. Sinter Lab, 211-LX) at 773 K and 50 MPa for 5 minutes. This composition is denoted as $Ge_{0.9}Sb_{0.1}Te$-BM+SPS in the main manuscript and Supporting Information.

Powder X-ray Diffraction (PXRD). Room temperature powder X-ray diffraction (PXRD) patterns for all the samples (GeTe, $Ge_{0.9}Sb_{0.1}Te$-ingot, and $Ge_{0.9}Sb_{0.1}Te$–BM+SPS) were recorded in a Rigaku Smartlab SE diffractometer using Cu Kα radiation (λ=1.5406 Å). The lattice parameters for pristine GeTe and $Ge_{0.9}Sb_{0.1}Te$-ingot are found to be $a= b=$ 4.166 Å and c = 10.673 Å, and $a= b=$ 4.201 Å and c = 10.592 Å respectively. $Ge_{0.9}Sb_{0.1}Te$–BM+SPS sample exhibits lattice parameter of $a= b=$ c = 5.972 Å.

Transmission Electron Microscopy (TEM). TEM images of powder $Ge_{0.9}Sb_{0.1}Te$–BM were taken using a JEOL (JEM2100+) instrument (200 kV accelerating voltage). TEM studies of $Ge_{0.9}Sb_{0.1}Te$–BM+SPS were carried out using a FEI TECNAI G^2 T20 STWIN TEM operated at 200 kV. TEM sample was prepared by mechanical polishing, followed by ion beam polishing to achieve thin (thickness 20 - 80 nm) foil.

Field emission scanning electron microscopy (FESEM) in back-scattered electron (BSE) mode. FESEM-BSE images were taken using a ZEISS Gemini SEM – Field Emission Scanning Electron Microscope and Apreo 2S, SEM, thermoscientific microscope.

Differential Scanning Calorimetry (DSC). A METTLER-TOLEDO differential scanning calorimeter (DSC 822 e) was used to collet DSC data with a ramp rate of 1 K/min in N_2 atmosphere.

Thermal Conductivity. Thermal diffusivity, D, of the samples were measured by laser flash diffusivity method using a Netzsch LFA-457 in the 300−723 K temperature range under N_2 atmosphere. Coins with typical dimension of ∼10 mm diameter and less than 2 mm thickness were used for the measurements. Temperature dependent heat capacity, C_p, of GeTe was determined by comparing with a standard sample (pyroceram) in LFA-457 (Figure S9). The total thermal conductivity, κ_{tot}, was then estimated using the formula $\kappa_{tot} = D\rho C_p$, where ρ is the density of the samples which were found to be ~ 98 – 99 % of the theoretical value.

Electrical Transport. Temperature variation of electrical conductivity (σ) and Seebeck coefficient (S) of the samples were measured simultaneously using a ULVAC-RIKO ZEM-3 instrument under helium atmosphere in the 300-723 K temperature range. The typical dimension of sample used for this measurement was $\sim 2\times2\times8$ mm^3. The electrical and thermal transports were measured in same direction.

Hall Measurement. Room temperature carrier concentration were determined from Hall coefficient measurements with the instrument developed by Excel Instrument, India. The maximum applied magnetic field was 1T. Room temperature carrier concentration was estimated using the formula $1/e.R_H$, where e is the electronic charge and R_H is the Hall coefficient.

Positron Annihilation Lifetime (PAL) Spectroscopy. The positron lifetime experiment has been carried out with a gamma-gamma coincidence technique. Here a 2.5 cm × 2.5 cm ultra-fast BaF_2 scintillator optically coupled with a XP 2020Q photomultiplier tube, is used as a gamma detector.[1, 2] The timing resolution of the present fast-fast coincidence setup is 220 ps measured with a ^{60}Co source with the proper positron window. A 10 μCi ^{22}NaCl positron emitting source, covered with a 6 micron thick mylar foil, has been used for the entire positron annihilation experiments. For a typical positron lifetime spectrum, about 10^7 coincidence counts have been recorded and deconvoluted with the PATFIT 88 software[3] with proper source correction.

The coincidence Doppler broadening (CDB) spectroscopy has been done with two identical (efficiency ~ 12%; type, PGC 1216sp of DSG, Germany) HPGe detectors having energy resolution of about 1.2 keV at 514 keV of ^{85}Sr.[4] The CDB data has been recorded in a dual ADC-based multiparameter data acquisition system, MPA-3 of FAST ComTec., Germany). The CDB spectra with ± ΔE selection, ensures a very high peak to background ratio (10^5: 1).[5] The CDB spectra has been analyzed by constructing the area normalized ratio curve with a pure Al single crystal.

Sound Velocity Measurement. The longitudinal (ν_l) and transverse (ν_t) sound velocities were measured on a disc-shaped sample by using an Epoch 650 Ultrasonic Flaw Detector (Olympus) instrument with the transducer frequency of 5 MHz. The mean sound velocity (ν_m) was estimated using the formula[6]:

$$v_m = \left(\frac{3}{v_l^{-3} + 2v_t^{-3}}\right)^{\frac{1}{3}}.$$

Calculation of the κ_{min} for GeTe. We have calculated the theoretical minimum thermal conductivity using Cahill's model by the equation: $\kappa_{min} = 1.21 n^{2/3} k_B \frac{1}{3}(2\nu_t + \nu_l)$, where k_B is the Boltzmann constant, ν_t and ν_l are the transverse and longitudinal sound velocities respectively, and n represents the number density of atoms.[7, 8] For GeTe, the values of ν_t and ν_l are 1900 m/s and 3352 m/s respectively (Table S1). By using these values, we have estimated the κ_{min} of GeTe ~ 0.3 W/m K.

Device Fabrication. Typically, fabrication of the double leg thermoelectric device involves consolidation of the $Ge_{0.9}Sb_{0.1}Te$–BM powder along with the end layers of Cu/Fe using SPS at 470 ºC with 48 MPa for 5 min under vacuum to form the p-type leg. On the other hand, to prepare the n-type leg, we have consolidated $Pb_{0.997}In_{0.003}Te_{0.996}I_{0.004}$ [9] powder along with the end layers of Cu/Fe using SPS at 600 ºC with 45 MPa for 5 min under vacuum After cutting the legs in appropriate dimensions, the legs are bonded to 1 mm thick alumina base plate with Cu interconnects. Both the legs are connected to Cu plate by a Zn layer. The arrangement of different layers in the fabricated double leg device is schematically shown in Figure 7b. Power generating properties of the fabricated device was estimated by mini-PEM module testing system (Advance Riko).[10-13]

Computational details. Our first-principles electronic structure calculations are performed within the framework of density functional theory (DFT) using generalized gradient approximation

(GGA) of the Perdew-Burke-Ernzerhof (PBE)[14] form for the exchange-correlation functional as implemented in the Vinea Ab-initio Simulation Package (VASP).[15] The projector augmented wave (PAW)[16] pseudo-potentials are used to describe the core electrons. Electronic wave-functions are expanded using plane waves up to a cut-off energy of 600 eV. A supercell (2 ×2 × 2) of Ge_8Te_8 was constructed to describe 12.5% Sb doping (Ge_7SbTe_8) based on the primitive GeTe cell. The Monkhorst-Pack *k*-mesh is set to 11 × 11 ×11 (6 ×6 × 6) in the Brillouin zone for the self-consistent calculation of primitive unit-cell (supercell), and all atoms are relaxed in each optimization cycle until atomic forces on each atom are smaller than 0.01 eV/Å. Spin-orbit coupling has been included for the band-structure calculations.

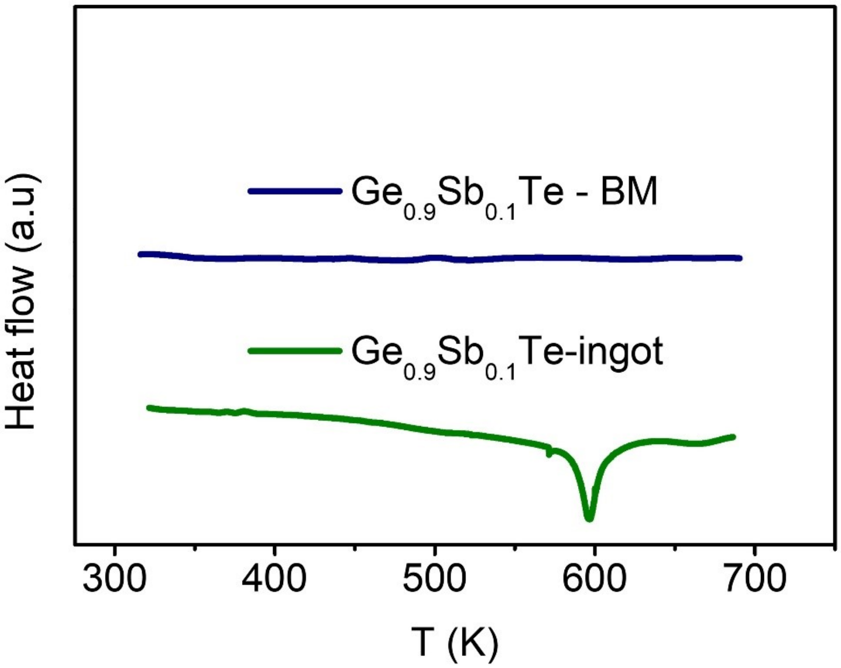

Figure S1. DSC curve of $Ge_{0.9}Sb_{0.1}Te$-ingot and $Ge_{0.9}Sb_{0.1}Te$–BM+SPS.

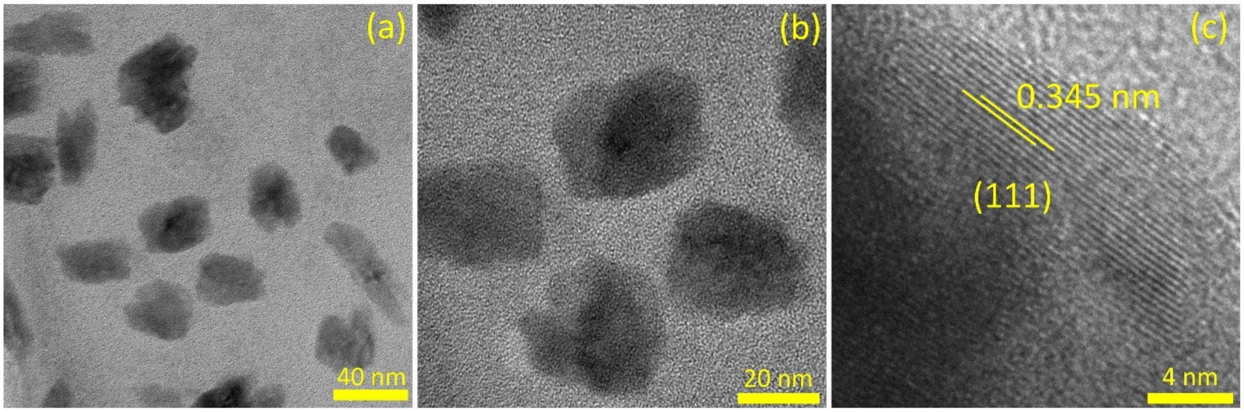

Figure S2. (a) and (b) TEM images of $Ge_{0.9}Sb_{0.1}Te$–BM powder showing the ~20-40 nm sized particles obtained after high energy ball milling. (c) HRTEM image exhibiting *d*-spacing of 0.345 nm which corresponds to the (111) plane of the cubic structure of GeTe.

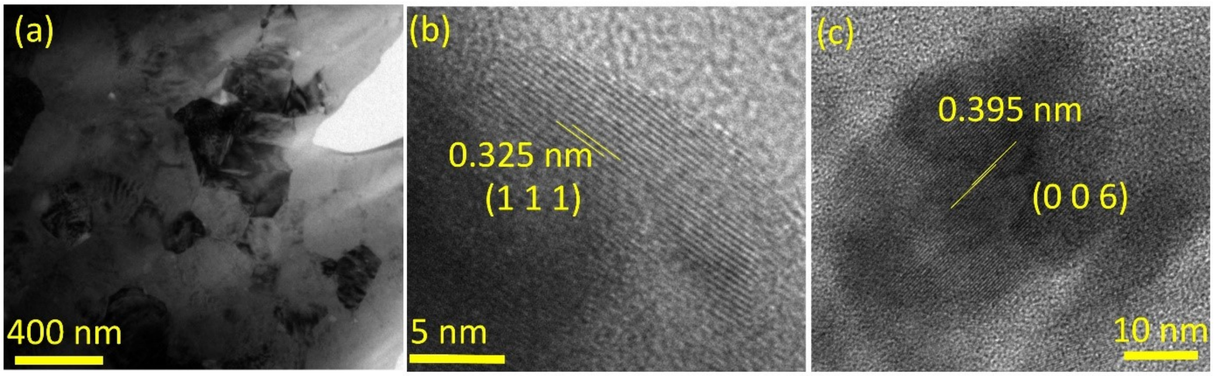

Figure S3. (a) Low magnification TEM image of $Ge_{0.9}Sb_{0.1}Te$-BM+SPS sample showing the presence of nano/mesoscale grains. HRTEM images of the nanoprecipitates shown in (b) and (c) with *d*-spacing 0.325 nm and 0.395 nm corresponding to the (111) and (006) planes of Ge and $GeSb_4Te_7$, respectively.

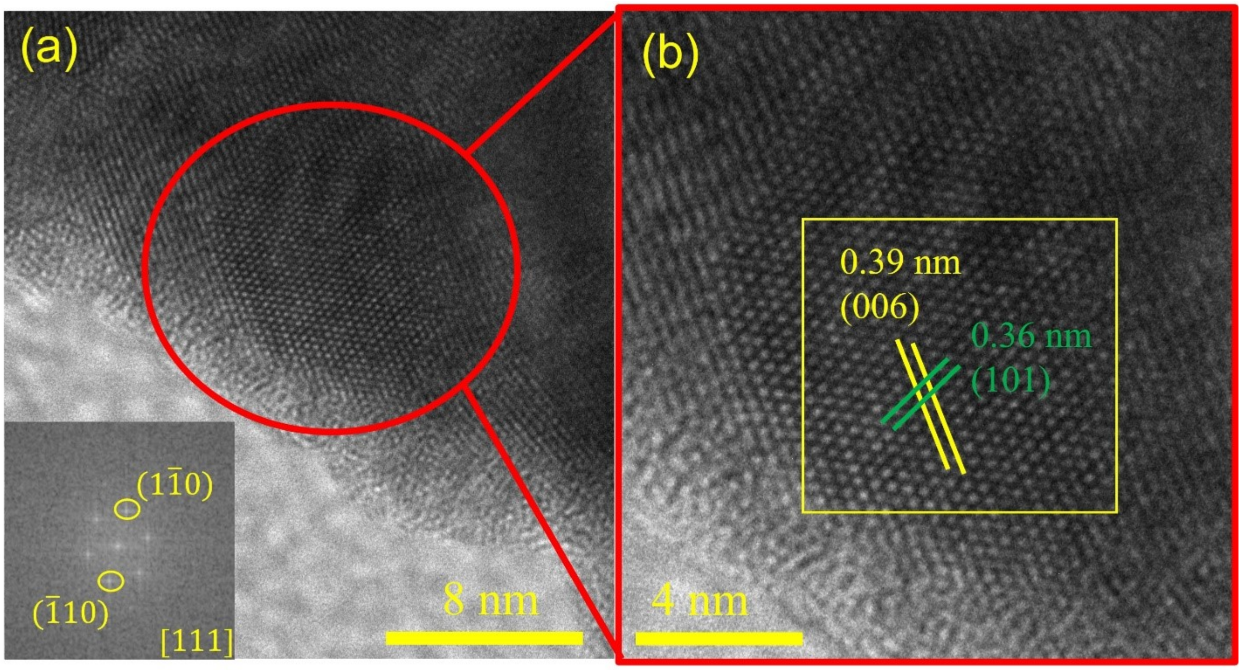

Figure S4. (a) HRTEM image of the $GeSb_4Te_7$ nanoprecipitate in GeTe matrix. (b) A zoomed in image of the red encircled portion of (a). The *d*-spacing in (b) having values of 0.39 nm and 0.36 nm corresponds to the (006) and (101) planes, respectively, of $GeSb_4Te_7$. The inset of (a) shows the fast Fourier transformation (FFT) image of the yellow boxed portion in (b), which is in accordance with the hexagonal structure of $GeSb_4Te_7$.

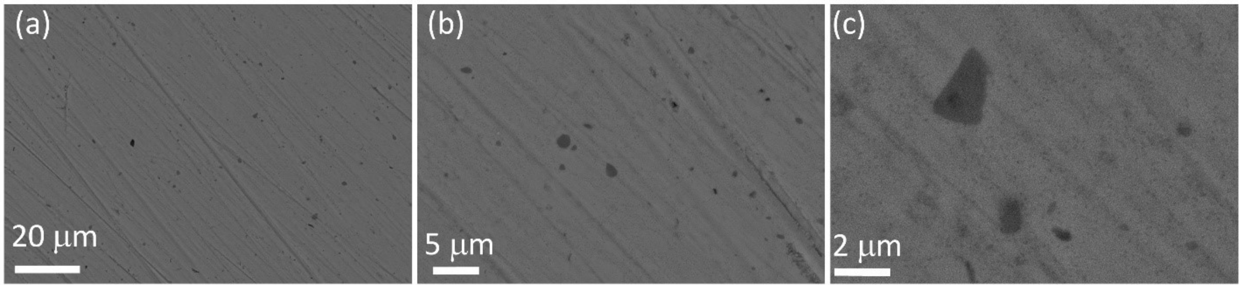

Figure S5. (a), (b), (c) BSE-FESEM images of $Ge_{0.9}Sb_{0.1}Te$–BM+SPS pellet with different magnification.

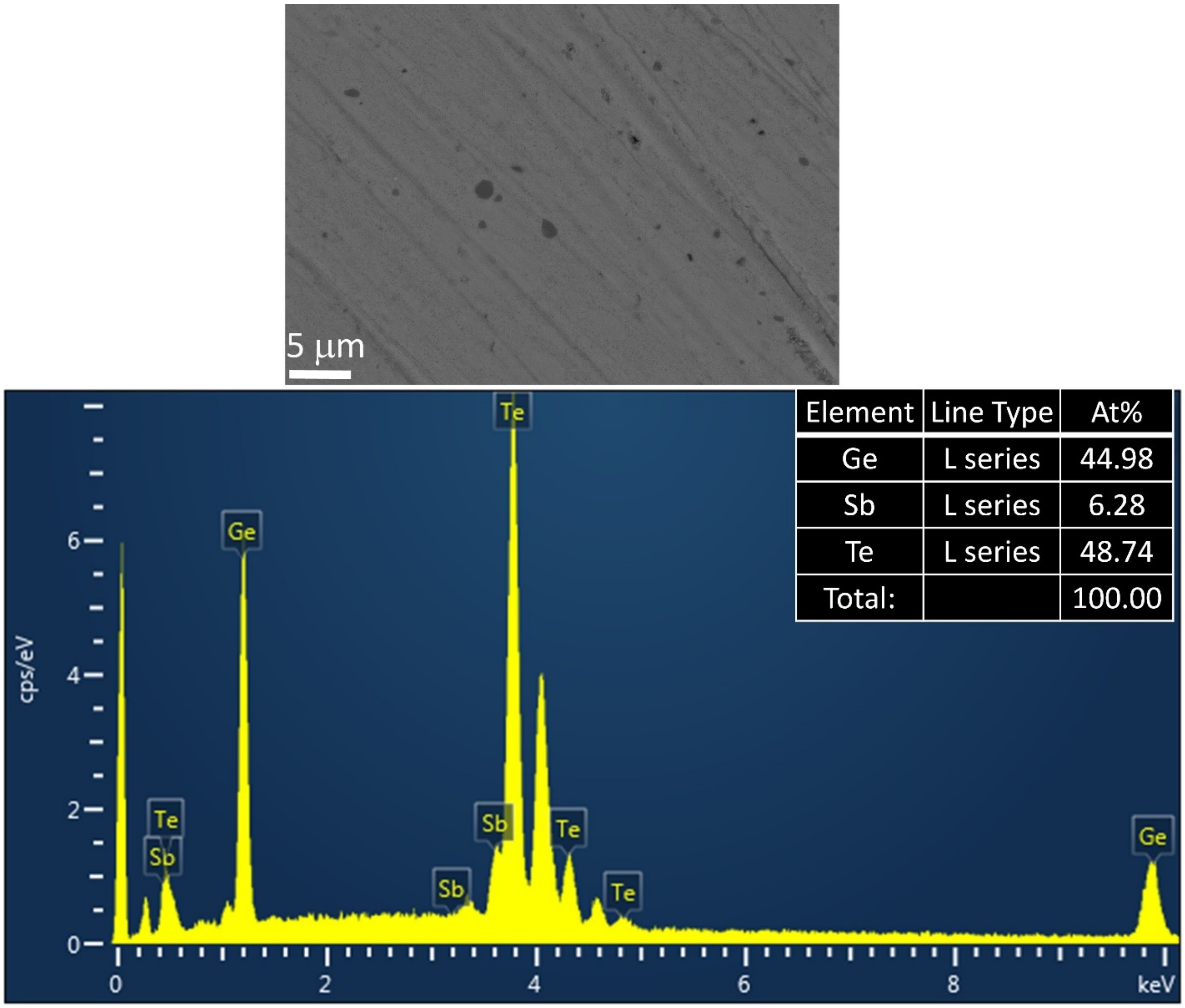

Element	Line Type	At%
Ge	L series	44.98
Sb	L series	6.28
Te	L series	48.74
Total:		100.00

Figure S6. Typical BSE-FESEM image of $Ge_{0.9}Sb_{0.1}Te$–BM+SPS pellet with corresponding EDAX spectra shows that the constituent elements Ge, Sb and Te, are present close to their nominal composition in the sample.

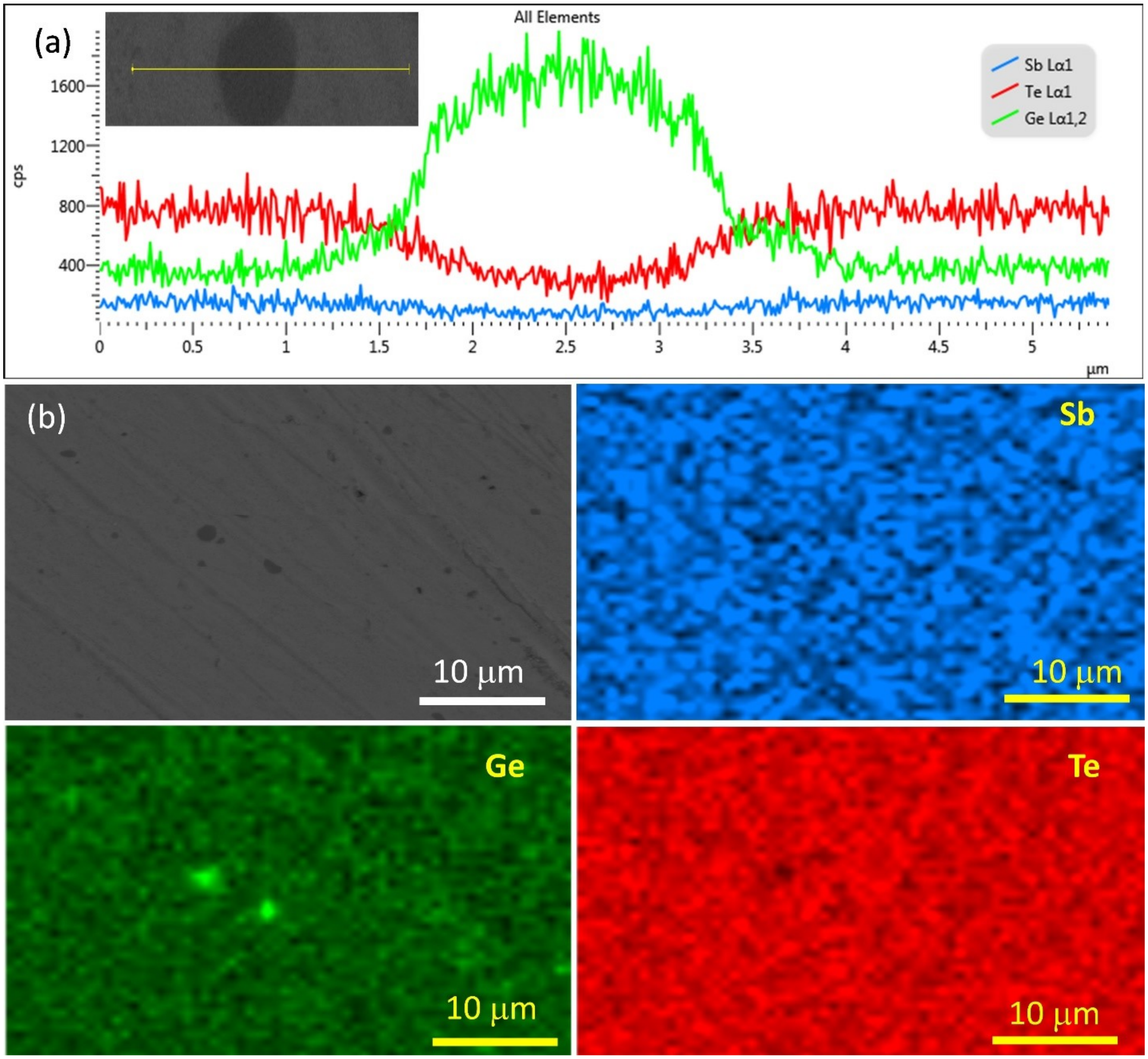

Figure S7. (a) EDAX line scan (yellow line in (a)) demonstrating the Ge rich nature of the micro-precipitate in $Ge_{0.9}Sb_{0.1}Te$–BM+SPS pellet. (b) Elemental color mapping of Ge, Sb and Te showing the precipitates are Ge rich.

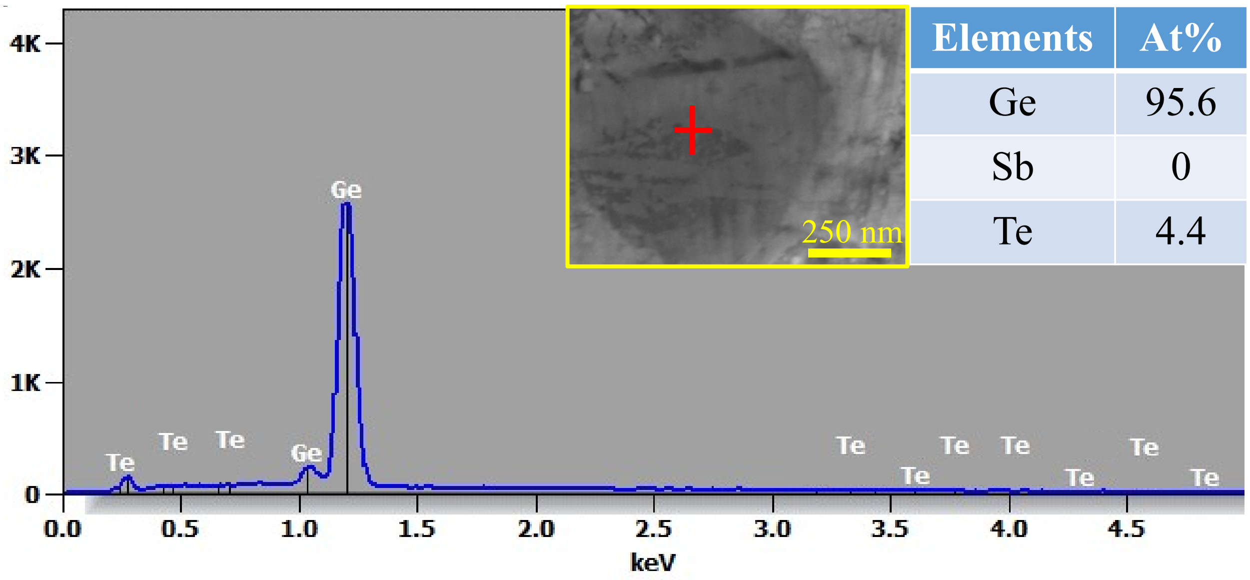

Elements	At%
Ge	95.6
Sb	0
Te	4.4

Figure S8. Typical EDAX spectra of $Ge_{0.9}Sb_{0.1}Te$–BM+SPS pellet taken on the point indicated with red cross inside the micro precipitate demonstrating that the microprecipitates are of Ge in the $Ge_{0.9}Sb_{0.1}Te$ matrix.

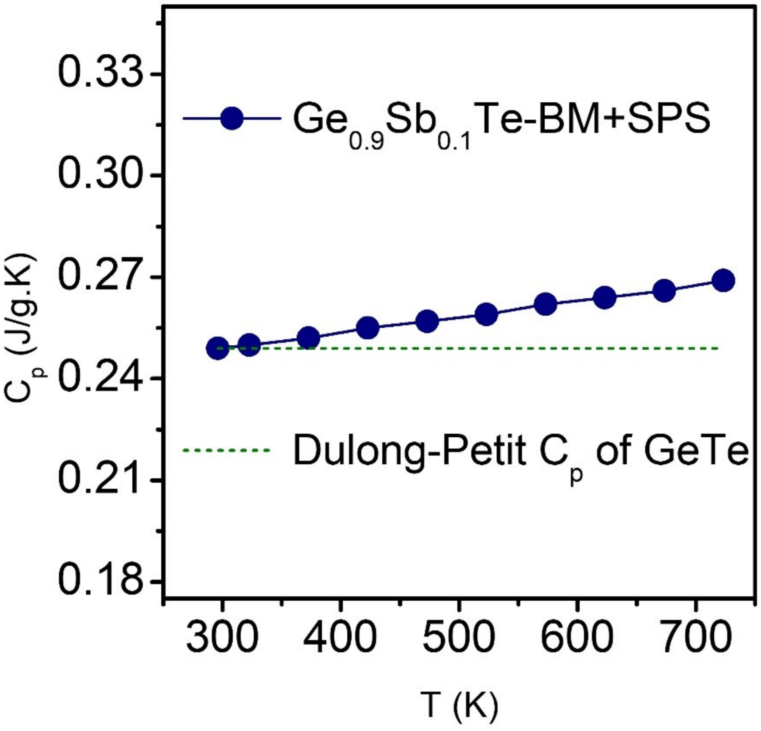

Figure S9. Temperature dependent heat capacity (C_p) of $Ge_{0.9}Sb_{0.1}$Te-BM+SPS.

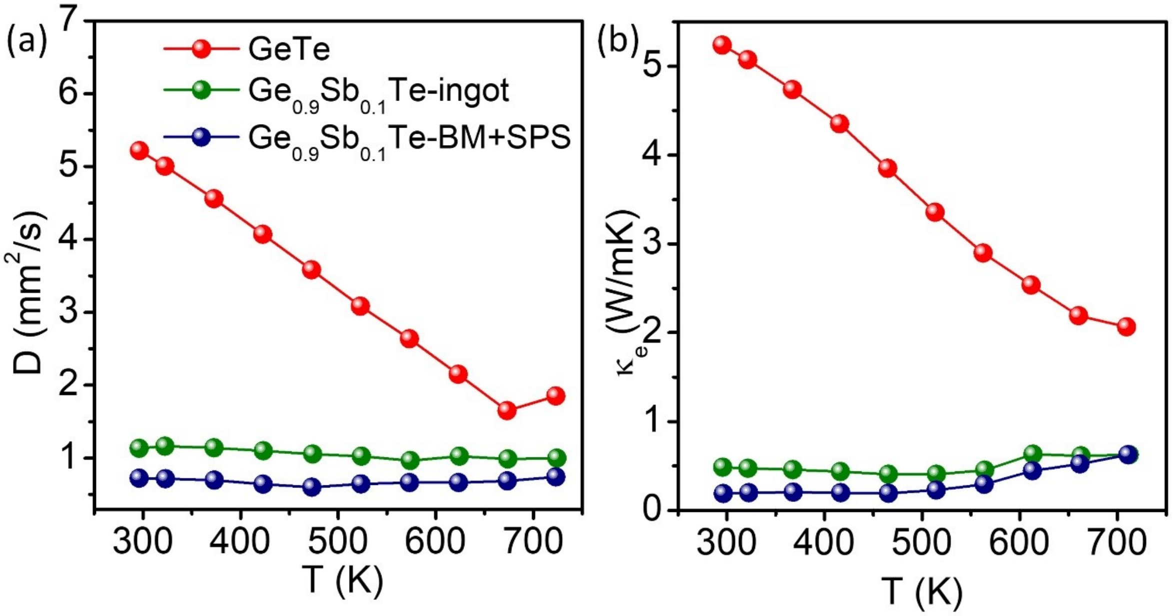

Figure S10. Temperature variation of (a) thermal diffusivity (D) and (b) electronic thermal conductivity (κ_e) of GeTe, $Ge_{0.9}Sb_{0.1}Te$-ingot, and $Ge_{0.9}Sb_{0.1}Te$ – BM+SPS.

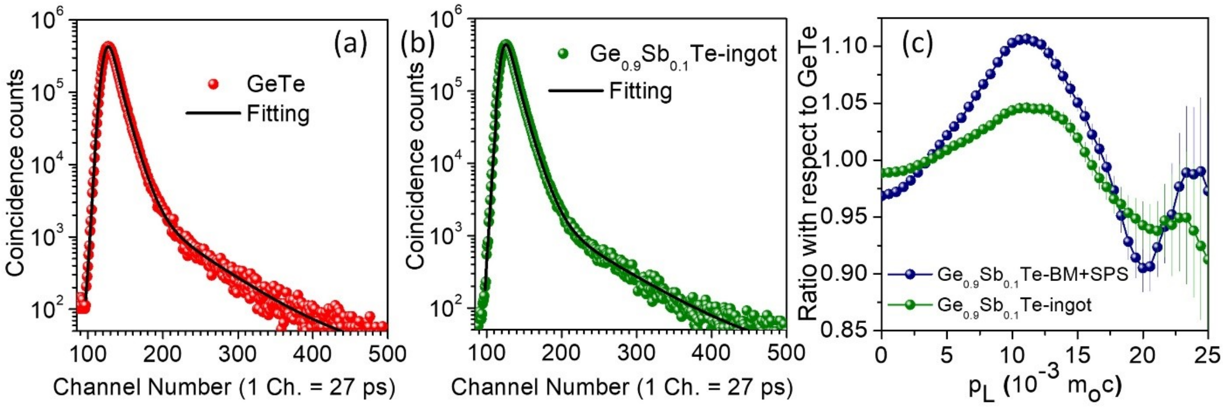

Figure S11. Positron annihilation lifetime spectra for (a) GeTe and (b) $Ge_{0.9}Sb_{0.1}Te$-ingot at room temperature. (b)The area normalized ratio curve of the CDB spectra of $Ge_{0.9}Sb_{0.1}Te$-ingot and $Ge_{0.9}Sb_{0.1}Te$-BM+SPS samples with respective to the CDB spectra of GeTe sample.

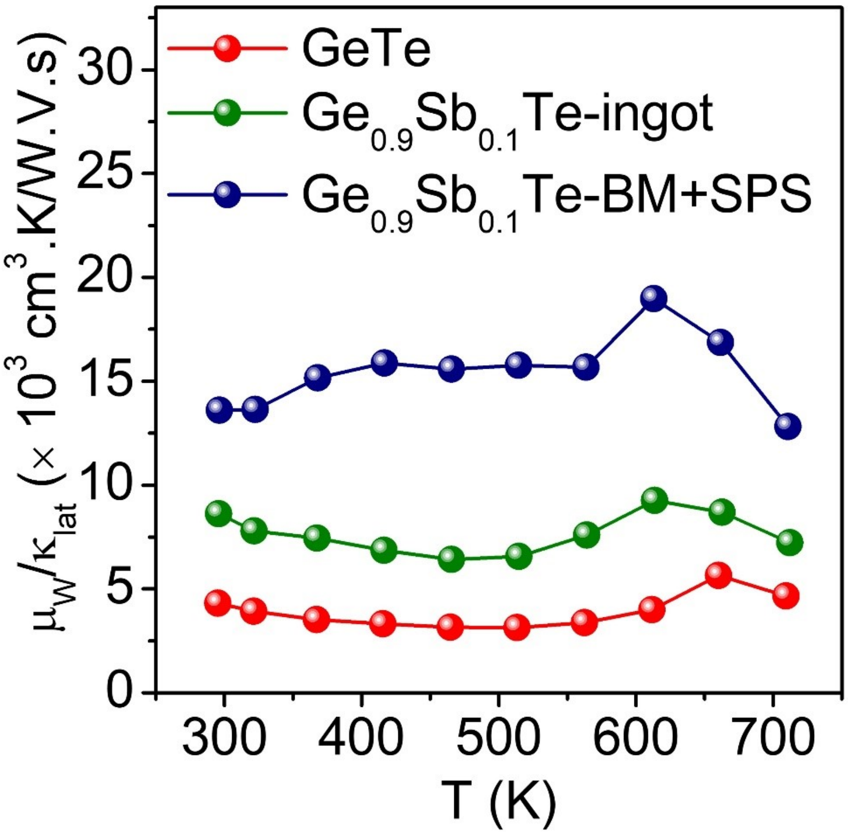

Figure S12. Temperature dependent weighted mobility (μ_w) to lattice thermal conductivity (κ_{lat}) ratio (i.e., μ_w/κ_{lat}) of GeTe, $Ge_{0.9}Sb_{0.1}Te$-ingot and $Ge_{0.9}Sb_{0.1}Te$–BM+SPS.

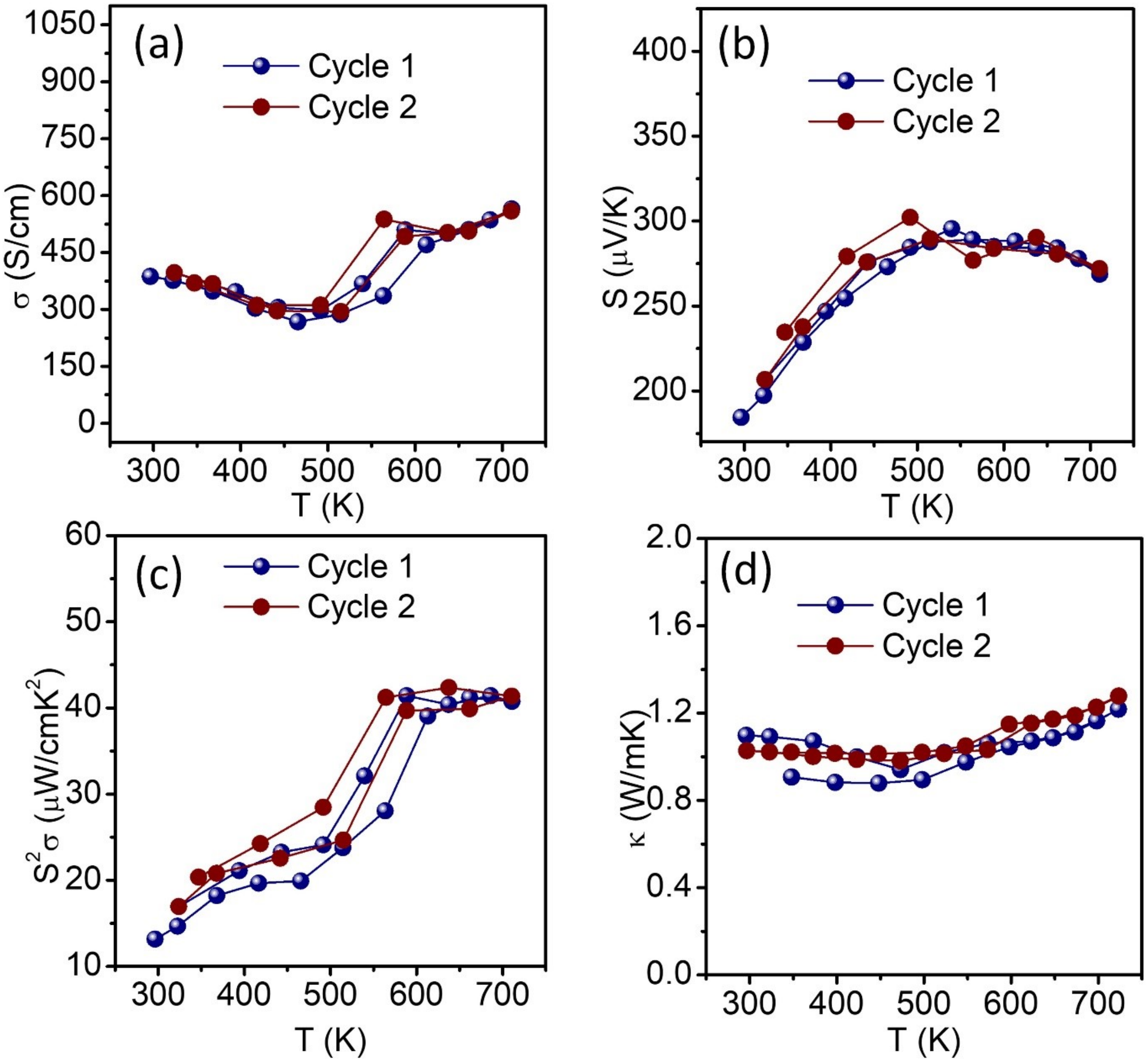

Figure S13. Temperature variation of electrical conductivity (σ), Seebeck coefficient (S), power factor ($S^2\sigma$) and total thermal conductivity (κ_{tot}) of $Ge_{0.9}Sb_{0.1}Te$–BM+SPS sample for multiple heating-cooling cycles exhibiting thermal stability at high temperature.

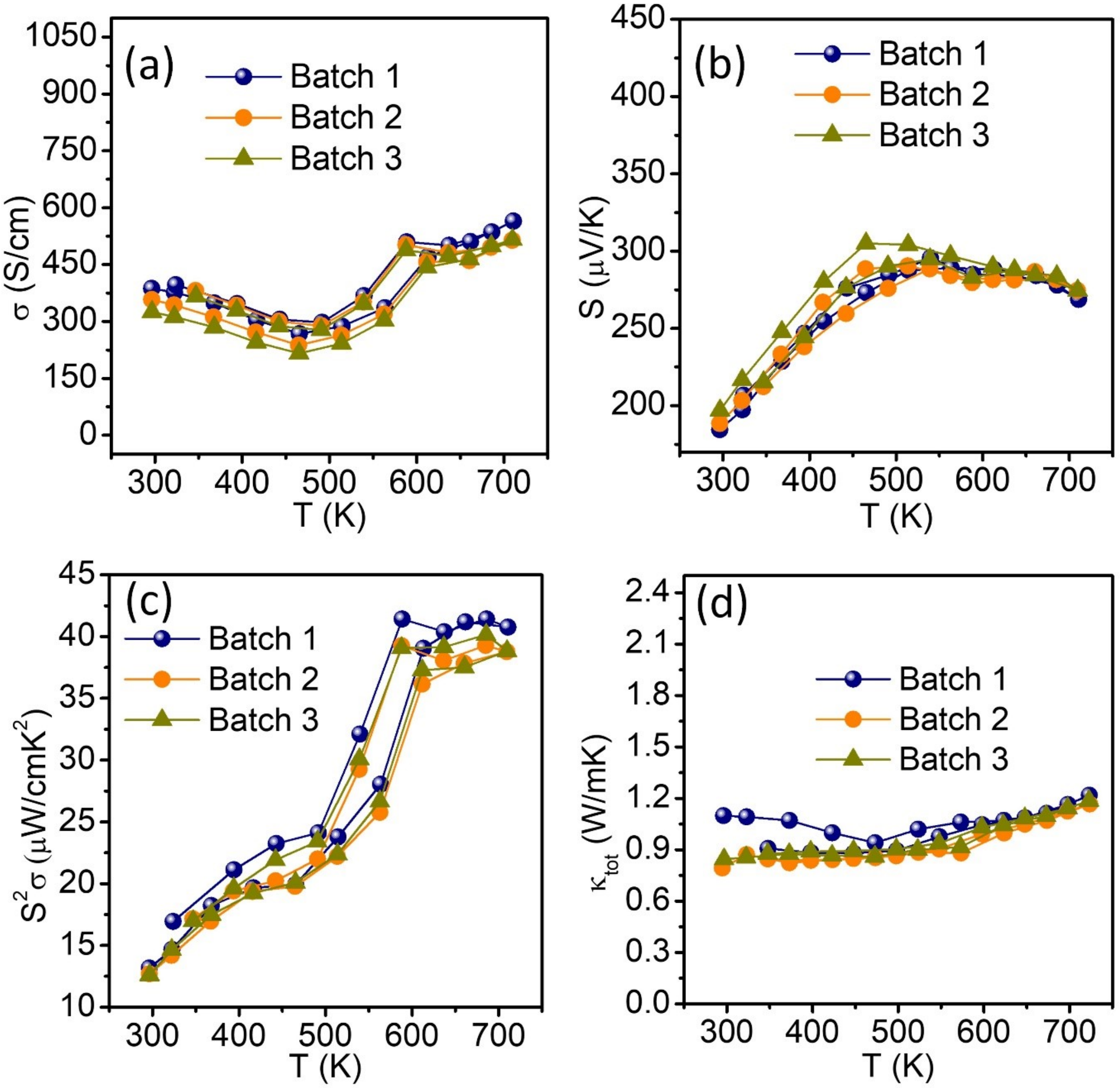

Figure S14. Temperature variation of electrical conductivity (σ), Seebeck coefficient (S), power factor ($S^2\sigma$) and total thermal conductivity (κ_{tot}) of three different batches of $Ge_{0.9}Sb_{0.1}Te$–BM+SPS samples showing the repeatability of the synthesis and measurements.

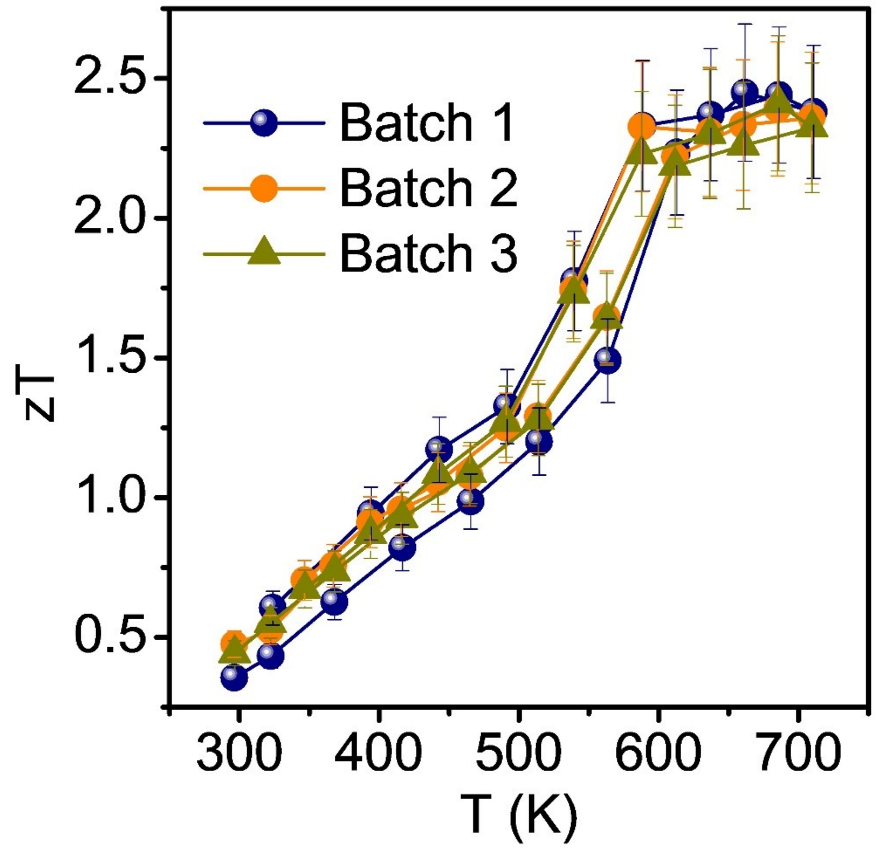

Figure S15. Temperature variation of thermoelectric figure of merit (zT) of three different batches of $Ge_{0.9}Sb_{0.1}Te$–BM+SPS samples showing the repeatability of the measurements. (The error bar is 10 %)

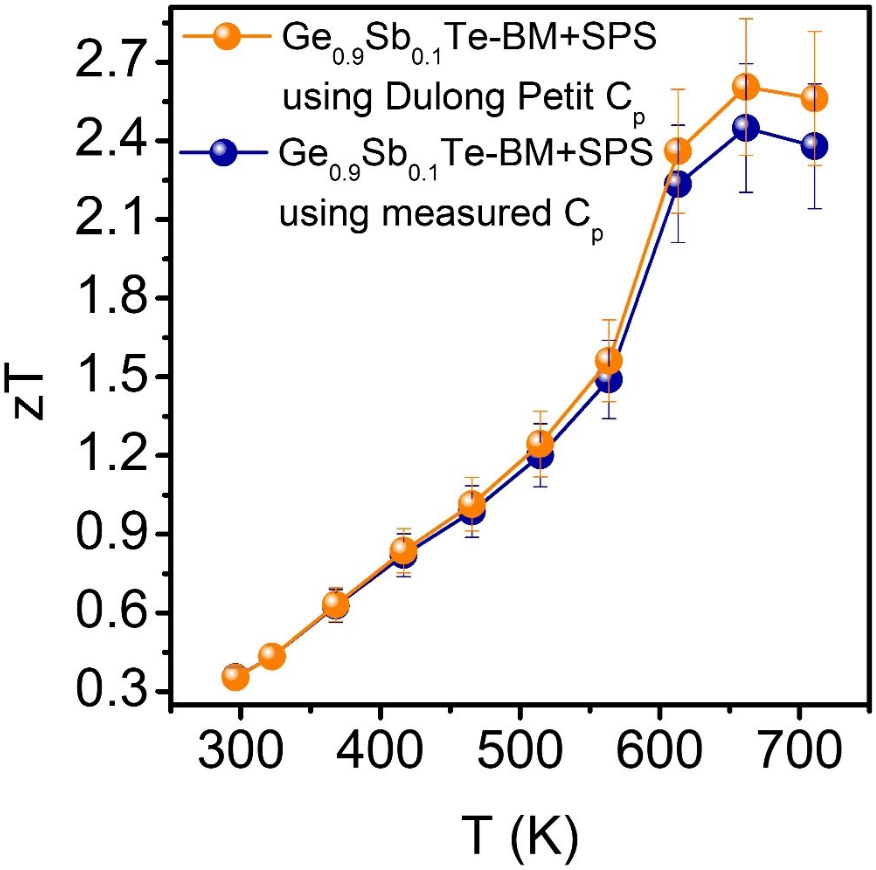

Figure S16. Temperature dependent thermoelectric figure of merit (zT) of $Ge_{0.9}Sb_{0.1}Te$–BM+SPS estimated using measured C_p and Dulong Petit C_p. (The error bar is 10 %)

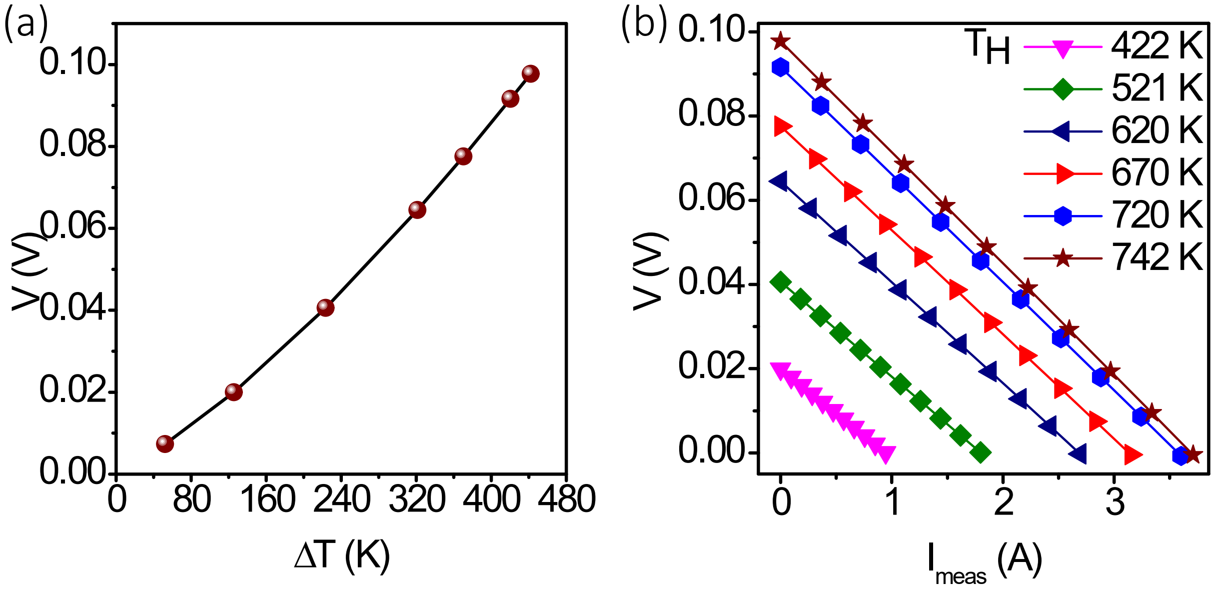

Figure S17. Variation of terminal voltage (V) as a function of (a) ΔT and (b) current (I_{meas}) at different T_H.

Table S1. Experimental sound velocities of GeTe, $Ge_{0.9}Sb_{0.1}Te$-ingot, and $Ge_{0.9}Sb_{0.1}Te$–BM+SPS at room temperature.

Sample	**Longitudinal** **v_l (m/s)**	**Transverse** **v_t (m/s)**	**Average** **v_m (m/s)**
GeTe	3352	1900	2112
$Ge_{0.9}Sb_{0.1}Te$-ingot	2905	1697	1882
$Ge_{0.9}Sb_{0.1}Te$–BM+SPS	2619	1454	1619

Table S2. Room temperature carrier concentration (*n*), hall carrier mobility (μ) and density of GeTe, $Ge_{0.9}Sb_{0.1}Te$-ingot, and $Ge_{0.9}Sb_{0.1}Te$–BM+SPS.

Sample	***n* (× 10^{20} cm^{-3})**	**Density (g cm^{-3}) (% of the theoretical density)**
GeTe	6.0	6.0 (98%)
$Ge_{0.9}Sb_{0.1}Te$-ingot	2.0	6.1 (99%)
$Ge_{0.9}Sb_{0.1}Te$–BM+SPS	0.86	6.1 (99%)

Table S3. Positron annihilation lifetime parameters in pristine GeTe, $Ge_{0.9}Sb_{0.1}Te$-ingot and $Ge_{0.9}Sb_{0.1}Te$–BM+SPS. The positron bulk lifetime (τ_B) is estimated from all the experimentally fitted parameters using the following formula $\tau_B = (I_1/\tau_1 + I_2/\tau_2)^{-1} \times (I_1 + I_2)$ where τ_2 is the positron lifetime in the defect site and its intensity I_2 is a measure of that particular defects in the sample.

Sample	**τ_1 (ps)**	**I_1 (%)**	**τ_2 (ps)**	**I_2 (%)**	**τ_3 (ps)**	**I_3 (%)**	**τ_B (ps)**	**κ_d (ps^{-1})**
GeTe	175 ± 3	31 ± 1	324 ± 5	67 ± 1	1683 ± 50	2 ± 0.1	255	1.79×10^{-3}
$Ge_{0.9}Sb_{0.1}Te$-ingot	206 ± 5	44 ± 1	351 ± 7	54 ± 1	1867 ± 100	2 ± 0.1	267	1.11×10^{-3}
$Ge_{0.9}Sb_{0.1}Te$–BM+SPS	204 ± 2	47 ± 1	352 ± 5	51 ± 1	1845 ± 70	2 ± 0.1	261	1.07×10^{-3}

References.

1. A. Sarkar, M. Chakrabarti, S. K. Ray, D. Bhowmick and D. Sanyal, *J. Condens. Matter Phys.*, 2011, **23**, 155801.
2. H. Luitel, A. Sarkar, M. Chakrabarti, S. Chattopadhyay, K. Asokan and D. Sanyal, *Nuclear Instruments and Methods in Physics Research Section B: Beam Interactions with Materials and Atoms*, 2016, **379**, 215-218.
3. D. Sanyal, D. Banerjee, R. Bhattacharya, S. K. Patra, S. P. Chaudhuri, B. N. Ganguly and U. De, *J. Mater. Sci.*, 1996, **31**, 3447-3451.
4. H. Luitel, D. Sanyal, N. Gogurla and A. Sarkar, *J. Mater. Sci.*, 2017, **52**, 7615-7623.
5. K. G. Lynn and A. N. Goland, *Solid State Commun.*, 1976, **18**, 1549-1552.
6. E. Rathore, R. Juneja, S. P. Culver, N. Minafra, A. K. Singh, W. G. Zeier and K. Biswas, *Chem. Mater.*, 2019, **31**, 2106-2113.
7. M. T. Agne, R. Hanus and G. J. Snyder, *Energy Environ. Sci.*, 2018, **11**, 609-616.
8. D. G. Cahill, S. K. Watson and R. O. Pohl, *Phys. Rev. B*, 1992, **46**, 6131-6140.
9. Q. Zhang, Q. Song, X. Wang, J. Sun, Q. Zhu, K. Dahal, X. Lin, F. Cao, J. Zhou, S. Chen, G. Chen, J. Mao and Z. Ren, *Energy Environ. Sci.*, 2018, **11**, 933-940.
10. H. Kunioka, A. Yamamoto, T. Iida and H. Obara, *Appl. Phys. Express*, 2017, **10**, 095801.
11. X. Hu, M. R. Barnett and A. Yamamoto, *J. Alloys Compd.*, 2015, **649**, 1060-1065.
12. S. Roychowdhury, T. Ghosh, R. Arora, M. Samanta, L. Xie, K. Singh Niraj, A. Soni, J. He, V. Waghmare Umesh and K. Biswas, *Science*, 2021, **371**, 722-727.
13. P. Acharyya, S. Roychowdhury, M. Samanta and K. Biswas, *J. Am. Chem. Soc.*, 2020, **142**, 20502-20508.
14. J. P. Perdew, K. Burke and M. Ernzerhof, *Phys. Rev. Lett.*, 1996, **77**, 3865-3868.
15. G. Kresse and J. Furthmüller, *Phys. Rev. B*, 1996, **54**, 11169-11186.
16. G. Kresse and D. Joubert, *Phys. Rev. B*, 1999, **59**, 1758-1775.